Tellus (2005), 57A, 117–135
Printed in UK. All rights reserved

TELLUS

Rotor types associated with steep lee topography: influence of the wind profile

By ROLF F. HERTENSTEIN[1]* and JOACHIM P. KUETTNER[2], [1]*Colorado Research Associates division of Northwest Research Associates Boulder, Colorado 80303, USA;* [2]*National Center for Atmospheric Research Boulder, Colorado 80303, USA*

(Manuscript received 13 March 2004; in final form 20 September 2004)

ABSTRACT

Turbulent rotors in the lower troposphere are usually associated with high-amplitude lee waves. Two types of rotors have been observed. The first type, often visible as harmless-looking cumulus or cumulus fractus lines paralleling the mountain range, comprises a well-defined circulation under the crests of resonant mountain waves. This type of rotor contains moderate or severe turbulence and is often confined below the height of a frequently-observed upstream, near-mountain-top inversion. A second, less common, rotor type extends much higher than the upstream inversion. This type has been observed to contain severe or extreme turbulence, and is thought to be associated with a high-amplitude mountain-wave system resembling a hydraulic jump. Both rotor types present a hazard to aviation, although the second type of rotor is far more dangerous.

We present high-resolution two-dimensional simulations of two distinct rotor types, which reveal dramatic differences in internal structure and turbulence intensity. The evolution of the lee-side horizontal vorticity provides insight into the formation mechanism involved. Horizontal vorticity within the initial upstream inversion is modified due to baroclinic generation as the flow spills down the lee slope. The magnitude of the modified horizontal vorticity is regulated by shear in the initial upstream inversion. At the same time, horizontal vorticity of the opposite sign forms in a shallow surface layer. The type of rotor that forms depends on the sign of the dominant horizontal vorticity as near-surface flow separation occurs along the lee slope. The simulations point to the vital role of an upstream near-mountain-top inversion, its deformation in the lee of the mountain, and the initial vertical shear within the inversion in rotor formation.

1. Introduction

Lower-tropospheric turbulence is frequently associated with mountain waves and can be as violent as any found in the atmosphere, leading to pilot reports of severe or even extreme turbulence (Lester, 1994). A schematic diagram of a mountain-wave system (Fig. 1) shows the wave flow itself (usually quite laminar) and turbulence in lower levels. The most intense observed turbulence occurs along the upwind side of the circulation shown under the roll cloud of the first wave crest. This conceptual model is idealized and does not apply to all mountain waves. Flow around three-dimensional topography and/or convective effects (Worthington, 2002) can cause variations in both the mountain-wave and lower-tropospheric turbulent structure. None the less, the conceptual model in Fig. 1 forms a basis from which to understand features commonly found in the lee of mountains.

Herein, we are concerned primarily with rotor turbulence, which can extend vertically from the surface to mountain-top level and sometimes substantially higher. We will use the term 'rotor' to describe any turbulent flow below the laminar mountain wave, corresponding in Fig. 1 to the shaded region in lower levels to the lee of the mountain. In situations conducive to mountain waves and rotors, the turbulence structure of the atmospheric boundary layer is substantially altered. Rotors manifest themselves as turbulent eddies ranging in size up to a few kilometers, and with horizontal vorticity aligned generally parallel to the mountain range producing the mountain wave. Clearly, vortical circulations along with severe or extreme turbulence may also exist in other locations in the mountain-wave system, e.g. the upper-level horizontal vortex tubes studied by Clark et al. (2000). Although it is possible for mountain-wave activity to exist without rotors, or for rotors to exist without wave activity above (e.g. rotor streaming; Foerchtgott, 1949, 1969), the two phenomena are most frequently found together. In addition, glider flights through numerous rotors by both authors indicate that one strongly turbulent eddy, with distinct up and down branches, sometimes constitutes the entire rotor, while at other times no

---

*Corresponding author.
e-mail: herten@cora.nwra.com

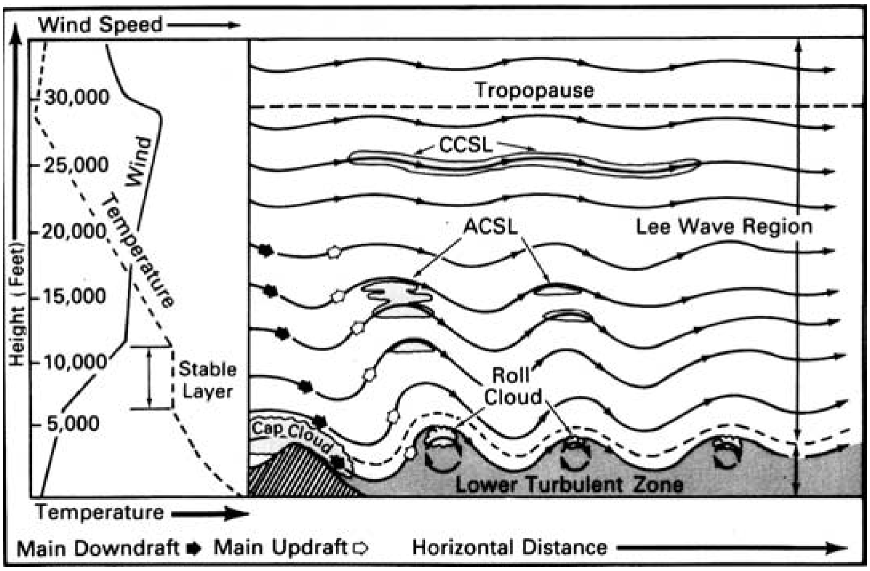

Fig 1. Schematic diagram of the mountain-wave system with resonant lee waves. The turbulent layer labeled 'Lower Turbulent Zone' in the lower troposphere and to the lee of the mountain is the focus of this study. Each 5000 ft on the height scale is 1524 m. The abbreviation CCSL indicates cirrocumulus standing lenticular, while ACSL shows altocumulus standing lenticular. (Reproduced with permission of Jeppesen Sanderson, Inc. Not to be used for navigation.)

organized circulation is encountered and only seemingly random areas of moderate or severe turbulence are found.

The first known mention of the rotor phenomenon was made by Koschmieder (1920) who photographed a rotor cloud and estimated a 10 m s^{-1} vertical motion on the leading edge of what he called the cloud roller. At the time, mountain waves were largely, if not completely, unknown.

The aviation hazards of rotors have been known since the 1930s. Both mountain waves and rotors were explored directly by aircraft during the Sierra Wave Project (SWP) in 1951–1952 and the Jet Stream Project (JSP) in 1955 (Holmboe and Klieforth, 1957; Grubišić and Lewis, 2004). During the latter project, a highly instrumented B-29 aircraft of the Air Force Cambridge Research Center flying near the 500-mb level (which is approximately 1.5 km above mountain-top level) penetrated an intense rotor in the lee of the Sierra Nevada Mountains. Flight data show 21 positive and negative vertical gusts reaching ± 20 m s^{-1} over 50 s (Fig. 2). To our knowledge, this is the only fully recorded penetration of a severe rotor. A few weeks later, during the JSP, a research glider broke apart while descending near the upwind side of another large and intense rotor (the renowned pilot, Larry Edgar, although injured, parachuted to safety). More recently, Kahn et al. (1997) have reported on a 1993 incident in which a Boeing 747–100 lost one engine in turbulence at about 600 m above ground level near Anchorage, Alaska. Their analysis indicates that rotor turbulence in the lee of the Chugach Mountains was likely responsible. Other aviation accident reports (e.g. National Transportation Safety Board, 1992) site rotors as a causal or contributing factor.

Kuettner (1959) used a model of the hydraulic jump to explain severe, high-reaching rotors observed during the SWP and JSP. He pointed to the importance of an upstream inversion that is almost always present in mountain-wave situations (Fig. 3) and also concluded that heating of the boundary layer played a role in observed rotors reaching heights of 7.5 km above the Owens Valley. This model contrasts markedly with the conceptual model of rotors associated with resonant waves shown in Fig. 1.

Lester and Fingerhut (1974) analyzed aircraft data from the Colorado Lee Wave Observing Program (Lilly and Toutenhoofd, 1969) and noted two distinct rotor types as well. The first type resembles the mountain-wave system shown in Fig. 1, with rotors containing moderate to severe turbulence. They parallel the mountain range, mark the position of lee waves overhead, and their typical height approximates that of the mountain top. Examples of rotor clouds with resonant waves in the lee of the Colorado Rocky Mountains are shown in Fig. 4. The second type of rotor is sometimes called the jump-type rotor because it has many characteristics of a hydraulic jump. As illustrated in Fig. 3, this rotor type extends well above the upstream inversion, and contains severe turbulence. Figure 5 shows an example of such vertically extensive rotor in the lee of the Sierra Nevada Mountains of California.

Despite the fact that rotors commonly occur in conjunction with mountain waves, of the approximately 1000 papers that have been written on mountain waves, only about 25 have dealt with rotors. A review of past observational and theoretical studies involving rotors can be found in Kuettner and Hertenstein (2002).

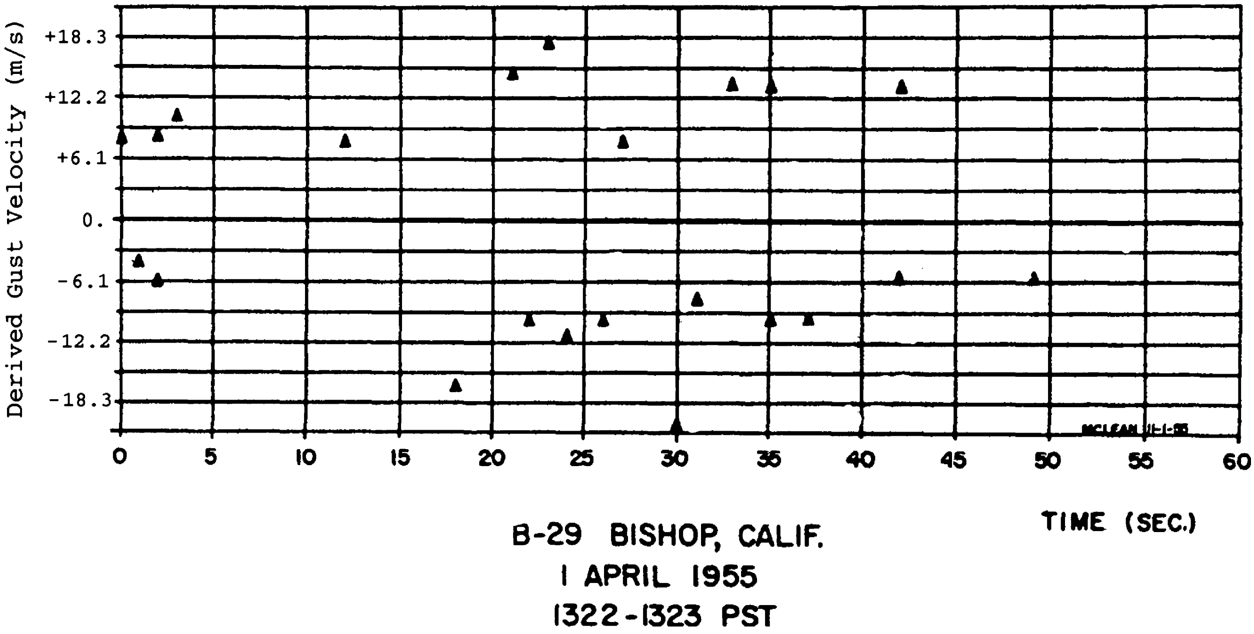

Fig 2. Vertical gusts measured by an Air Force B-29 aircraft that penetrated a severe rotor while flying at approximately 5300 m above sea level (3800 m above ground level) during the JSP (Holmboe and Klieforth, 1957).

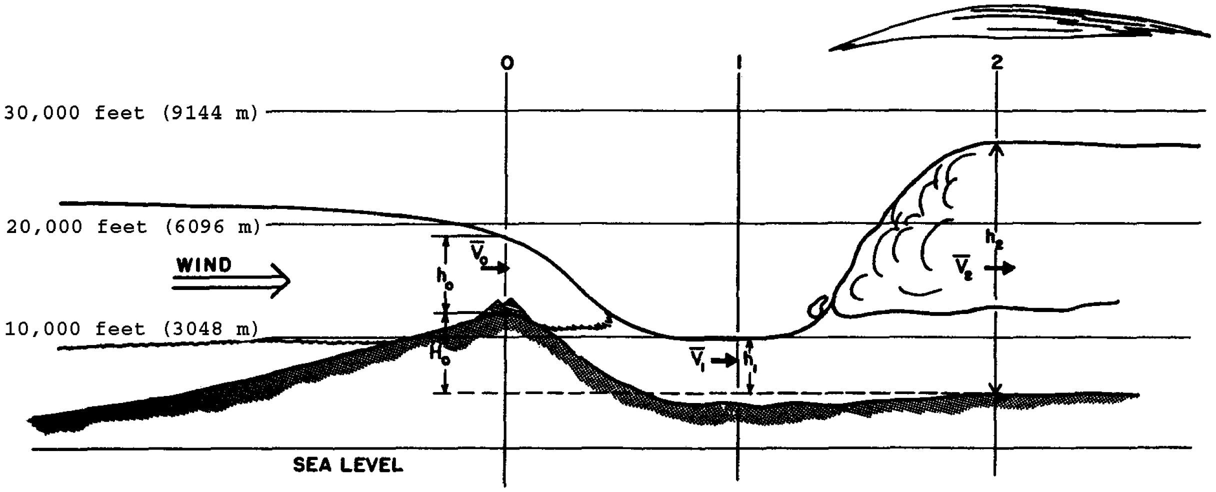

Fig 3. Schematic diagram of hydraulic-jump-like rotor system. Symbols h_0, h_1, and h_2 represent the inversion depth at three locations, while $\bar{v}_0$, $\bar{v}_1$, and $\bar{v}_2$ are average flow velocities in each layer. Note that the inversion depth after the jump (h_2) exceeds the upstream inversion depth (h_0). See Kuettner (1959) for additional details.

Recently, the rotor problem has received renewed interest. Doyle and Durran (2002, hereafter DD) report on a series of high-resolution, two-dimensional simulations used to explore the structure and development of rotors associated with resonant mountain waves. The authors found that surface-boundary-layer drag and lee-wave-induced adverse pressure gradients work together in rotor formation. In their simulations, a thin sheet of near-surface vorticity is lifted as the surface layer separates from the lower boundary, and appears to be responsible for the sign of the horizontal vorticity in the ensuing rotor.

A two-phase field program, the Terrain-Induced Rotor Experiment (T-REX) is planned for 2004 and 2006 in the Sierra Nevada Mountains and adjacent Owens Valley (Grubišić and Kuettner, 2003). Measurements taken during T-REX should greatly increase observational data on the internal structure of rotors.

Herein, we present two-dimensional simulations of two distinct rotor types formed downstream of mountains with steep lee-side topography. The simulation of one rotor type reveals characteristics that may help explain observed high-reaching, severe rotors. The spacing and quality of SWP and JSP

Fig 4. Two examples of the first type of rotor system showing rotor clouds associated with resonant waves in the lee of the Rocky Mountains near Boulder, Colorado. (a) Photograph taken 2 December 2003. Note the lenticular cloud topping the rotor cloud near the center of the photograph. (b) Photograph taken 29 December 2003. Note the lighter colored, deep Foehn or cap cloud in the distance. Photographs by R. Hertenstein.

Fig 5. Second type of rotor system showing high-reaching rotor clouds topped by lenticular clouds viewed from approximately 9800 m looking south along the Owens Valley. Wind direction is from the right. (Reproduced with permission of the photographer, T. Henderson.)

soundings, taken upstream of the Sierra Nevada and used for our model initialization, have left uncertainties regarding the magnitude of vertical wind shear through an almost ubiquitous near-mountain-top inversion. We discovered that relatively minor differences, especially in the magnitude of the shear through the inversion, lead to dramatic changes in the flow characteristics of the mountain wave and rotor downstream of the mountain.

The paper is organized as follows. Model details and simulation configuration are presented in Section 2. Results from the simulations demonstrating the striking difference between the two rotors types are shown in Section 3. An analysis of the formation mechanism using the evolution of horizontal vorticity in each simulation is found in Section 4. Sensitivity studies, which further demonstrate the role of wind shear through the near-mountain-top inversion, appear in Section 5. Conclusions are presented in Section 6.

2. Experimental design

Our two-dimensional simulations were performed with the Regional Atmospheric Modeling System (RAMS), which uses the non-hydrostatic, fully compressible governing equations. A terrain-following σ_z vertical coordinate in RAMS has been found effective for modeling atmospheric flows in steep terrain (e.g. Poulos et al., 2000). Complete details regarding model equations, vertical coordinate, grid structure, time and space differencing, as well as available parameterizations (e.g. radiation, turbulence, and microphysics) have been elaborated upon in Pielke et al. (1992) and numerous references therein.

A single model grid with horizontal grid spacing of 150 m was employed over 1700 points. Vertical spacing ranged from 20 m at the lowest level stretching to 150 m over 145 points to a maximum height of 19.7 km. The grid spacing is sufficient to resolve gross features of the simulated rotors but is not adequate for resolving decameter-scale turbulent eddies, which are implied by observations shown in Fig. 2. A sponge layer is applied to allay wave reflection at the upper boundary. A so-called ‘no-slip’ lower boundary condition was used. The scheme of Louis (1979) was followed to represent turbulence in the surface layer, specifically, vertical fluxes of horizontal momentum. Surface roughness over the entire domain was set to 0.1 m. At the lateral boundaries, the schemes of Klemp and Lilly (1978) and Durran and Klemp (1982) are applied, allowing energy to pass from the domain.

Topography was modeled with the well-known Witch of Agnesi profile. A two-sided profile was used due to the asymmetric, across-wind contour of the Sierra Nevada Mountains in California. A 40-km half-width on the upstream side and 5-km half-width on the lee side roughly approximate the profile of the Sierra Nevada, especially the lee slope. The mountain top in the model was located at 4000 m above sea level while topography drops to 1500 m above sea level away from the mountain. This specification of the model topography allows somewhat easier comparisons with SWP observations.

Simulations did not use a soil model or radiation parametrization, i.e. no heat is transferred from the surface. It has been shown by Kuettner (1959) and more recently by DD that surface heating will increase the height to which rotors extend but is not a primary factor in determining whether rotors will form. Simulations were also run with no moisture. Durran and Klemp (1982) have shown that moisture can modify resonant mountain lee waves; however, our results indicate that the structure and formation of the two rotor types can be understood using dry dynamics. The Deardorff (1980) scheme was used to parametrize turbulence above the surface layer (see also Section 5.2). High Rossby number flows simulated here justify neglect of the Coriolis force.

Horizontally homogeneous initialization was used, i.e. each simulation was initialized with a single vertical temperature and wind profile to describe the atmospheric state over the entire domain. The initial wind and temperature profiles were based on observations taken during the SWP and recollections of the second author (JK), who participated in the field campaign. In numerical experiments presented here, the temperature profile did not change but the initial wind profiles were varied to reflect

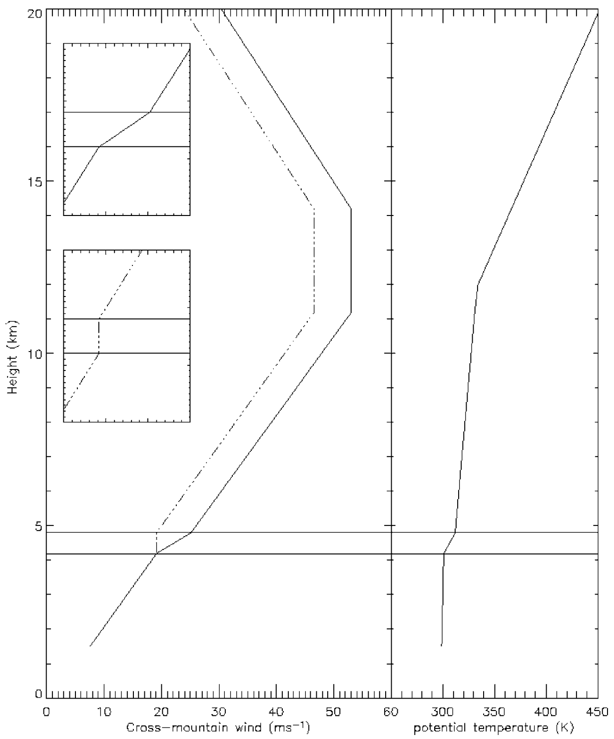

Fig 6. Initial wind profiles for S1 (solid) and S2 (dashed) and initial potential temperature. Insets expand the portion of each wind profile between 3 and 6 km. The upstream inversion (between 301 and 312 K) is indicated by the horizontal lines from 4.2 to 4.8 km in the main figure and in each inset.

observed conditions. A representative potential temperature profile (Fig. 6) is derived from upstream soundings at Oakland, Merced, and Santa Maria, California for 18 December 1951. A special (and partial) sounding taken at Lodge Pole, California, on that date was used to estimate the strength of the near-mountain-top inversion and the stability profile below the inversion. Scientists and pilots at the SWP classified this case as being a 'strong lee wave'. Wind profiles for the first rotor simulation (hereafter referred to as S1) and the second rotor simulation (hereafter referred to as S2) are also shown in Fig. 6. The first profile (S1, solid line) shows greater shear (13.3×10^{-3} s^{-1}) through the near-mountain-top inversion compared to the constant shear (4.29×10^{-3} s^{-1}) above and below, as was sometimes observed during the SWP. The second profile (S2, dashed line) uses the same shear above and below the inversion as S1, except there is zero shear through the near-mountain-top inversion. Such a wind profile occurred upstream of the Sierra Nevada on 25 April 1955, the date of a particularly severe rotor encounter described earlier. A so-called 'blunt' wind profile with an upper-level layer showing nearly constant winds was often observed in the vicinity of the tropopause during the SWP. Thus, the wind is held constant between 11.2 and 14 km, with negative shear (-3.9×10^{-3} s^{-1}) above this level. Details of actual upstream soundings were removed to simplify analysis and interpretation of results. Casual inspection of the two wind profiles would lead one to expect that S1 would produce the more violent rotor due to higher average winds in the troposphere. As we will see, this is not the case.

A sensitivity experiment was run in which we duplicated the model configuration, topography, and initial sounding used by DD. Results using RAMS were similar to those in DD.

3. Simulations of the two rotor types

In this section, we present results from S1 and S2 which clearly show the distinction between two simulated rotor types. Results of the model integration at three hours are shown, by which time the simulations had reached a quasi-steady state.

Isentropes for simulations S1 and S2 reveal the remarkable differences in flow regimes. Figure 7a shows a well-mixed rotor with near neutral stability extending vertically to approximately 4 km. Note that the undulating inversion remains intact in the lee of the mountains. We will refer to this type of rotor as Type 1. By contrast, isentropes at three hours for S2 reveal a mountain wave and rotor resembling a hydraulic jump (Fig. 7b). The turbulent rotor extends vertically to almost 8 km, substantially higher than S1, and turbulent flow several kilometers deep extends downstream for more than 50 km. We will refer to this type of rotor as Type 2.

A distinguishing feature of the Type 2 rotor is the splitting inversion that occurs near the bottom of the lee slope ($x = 23$ km), which may help explain the greater height of this rotor from a reduced gravity perspective. Kuettner (1959) noted that a reduction in the inversion on the lee side of the mountain allows the jump to extend to greater heights as the gravitational constraint on the inversion surface is eased. Smith (1987) found evidence of inversion splitting during bora events in Yugoslavia. In those cases, the inversion splits as the flow begins its descent down the lee slope, rather than near the bottom of the lee slope as in our simulations. We suspect that stronger negative horizontal vorticity in the vicinity of the jump (see discussion below) plays a role in the splitting; however, we do not yet fully understand the mechanism involved.

Motion pictures taken during one SWP case, thought to be a Type 2 rotor, indicate smaller cumulus fractus clouds forming directly upstream of the main rotor cloud leading edge, then propagating back into the main rotor cloud on a time-scale estimated to be 10 min. An animation of S2 offers a possible explanation for this observed phenomenon. Numerous individual eddies form at the leading edge of the rotor and subsequently grow, then dissipate as they propagate downstream in the turbulent flow. Three such eddies are indicated by '+' in Fig. 7b. These eddies generally propagate 2–5 m s^{-1} slower than the average wind speed near the top of the rotor and modify the overlying wave flow on short [O (min)] time-scales.

Streamlines over a smaller portion of the model domain and centered on the rotors further illustrate the two flow regimes

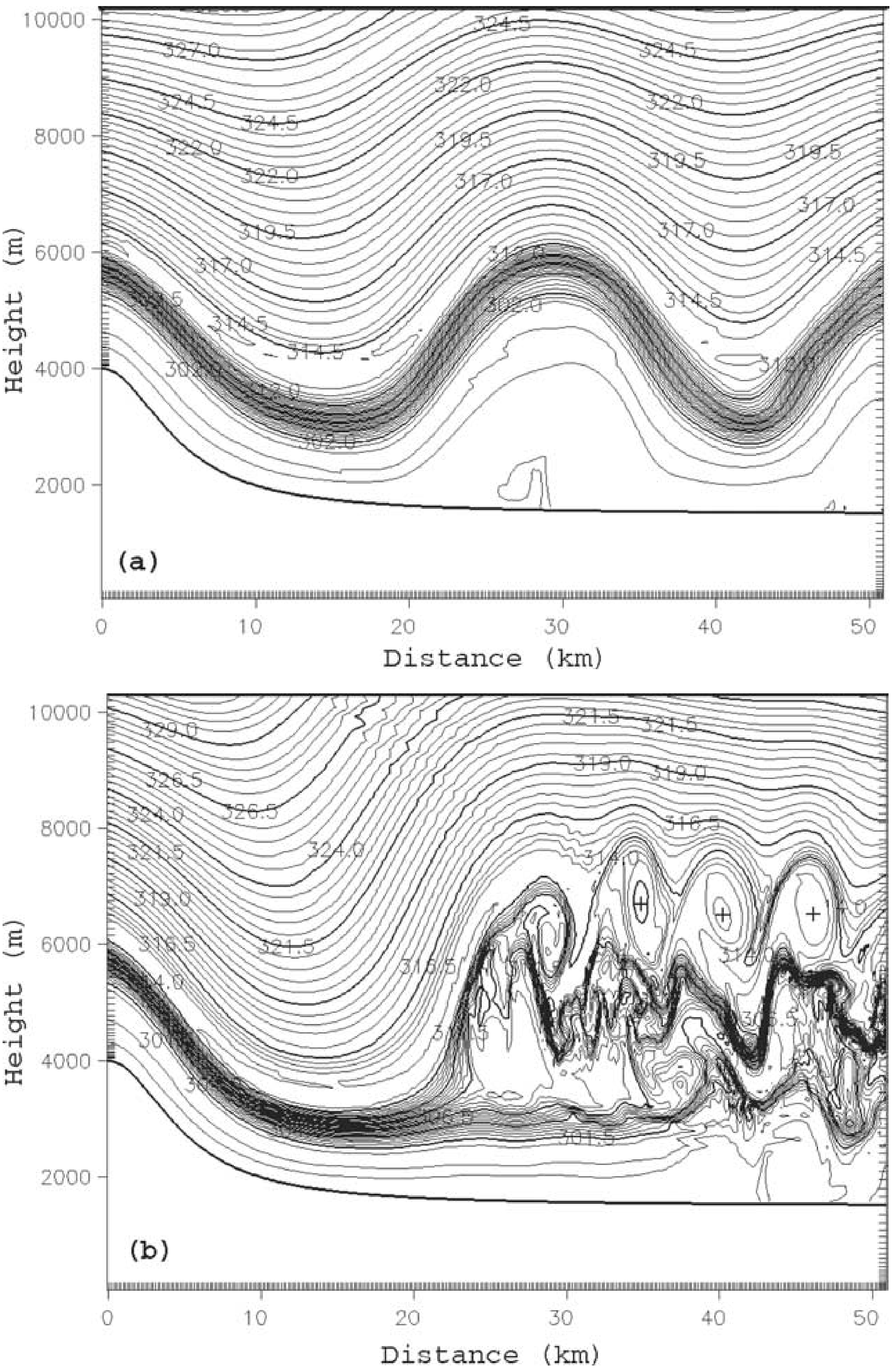

Fig 7. Potential temperature (contour interval 0.5 K) after three simulation hours for (a) Type 1 rotor (S1) and (b) Type 2 rotor (S2). Note the height of the Type 2 rotor as well as the splitting inversion at the jump. Three propagating eddies along the top of the Type 2 rotor are marked with ‘+’.

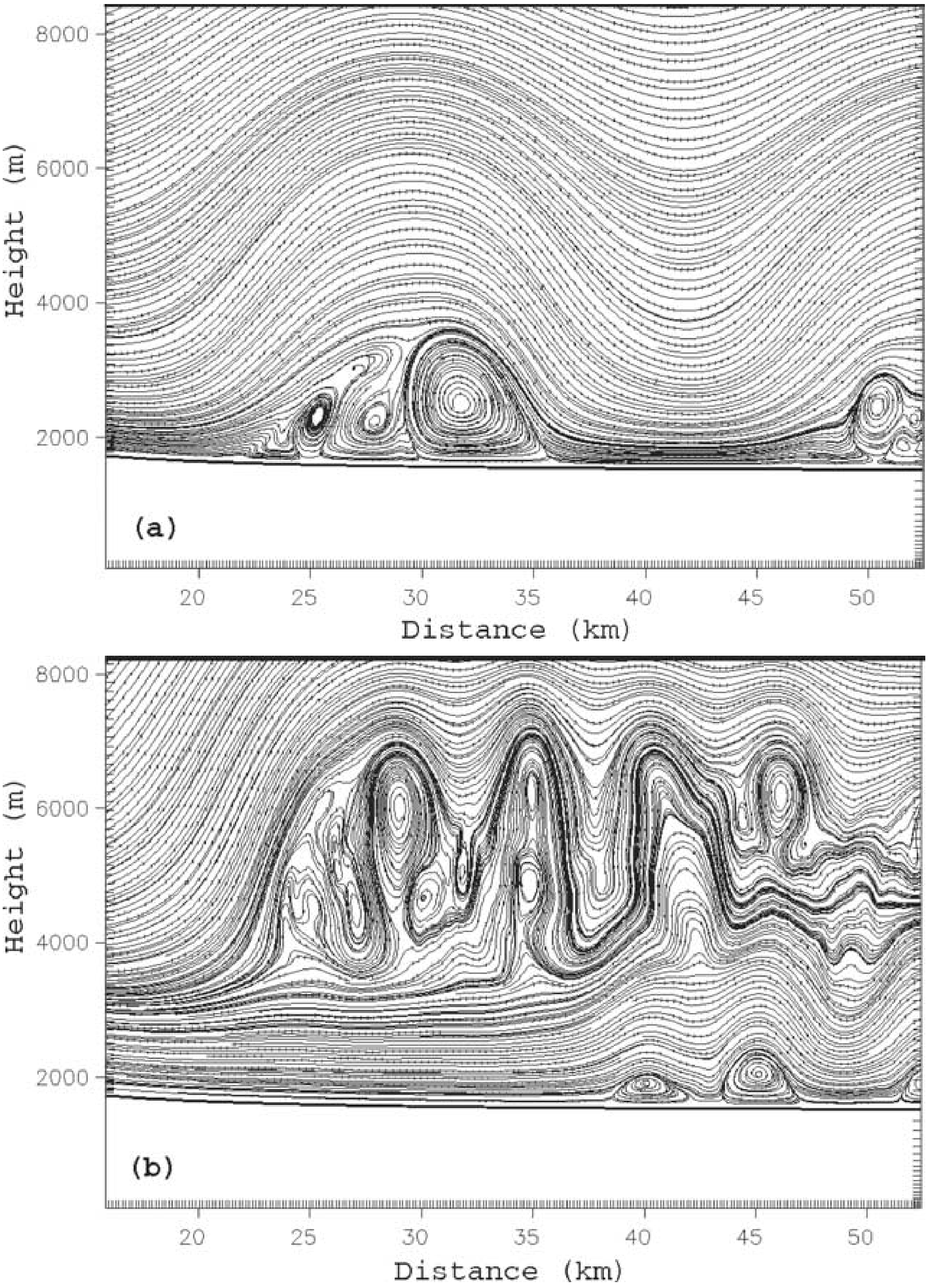

Fig 8. Streamlines illustrating the dramatic difference in flow structure between (a) the Type 1 rotor simulation and (b) the Type 2 rotor simulation. A smaller portion of the domain is shown in order to focus on details of the rotor.

(Fig. 8). In S1, three turbulent eddies are confined below approximately 3.8 km. The overall rotor remains nearly stationary, but individual eddies evolve over time within the rotor. Observations by Ralph et al. (1997) also indicate the presence of more than one eddy in a rotor under resonant waves in the lee of the Colorado Rocky Mountains. By contrast, eddies in S2 are elevated well above the surface and extend to 7.5 km. While the Type 2 rotor leading edge remains at approximately $x = 23$ km, the eddies within the rotor are in a continual state of turmoil.

Doyle and Durran (2003) present results from very high-resolution, three-dimensional simulations with variations in the across-wind topography. The simulation exhibits a 'parent' rotor under the first mountain-wave crest within which several 'subrotors' evolve. The subrotors are of the order of a kilometer in size and have lifetimes of 5–10 min. The individual eddies within both our simulated rotor types are several times larger in space and time; we have not simulated subrotors on the scale of those of Doyle and Durran 2003.

Additional insight into the differences between rotor types can be gleaned by inspection of the horizontal and vertical flows. Horizontal velocity (u) for S1 shows the resonant wave pattern as well as reversed flow in the rotors under the first wave crest (Fig. 9a). Downslope flow reaches 43 m s^{-1} and extends 20 km from the mountain top. By contrast, downslope flow in S2 reaches 53 m s^{-1} and extends almost twice as far from the mountain top (Fig. 9b). Additionally, the strong near-surface flow in S2 first undercuts the turbulent rotor flow before itself undulating and also breaking down into low-level eddies. In the turbulent rotor, elevated regions of reverse flow appear in several areas, some reaching -8 m s^{-1}. Near the top of the rotor, the downstream-traveling eddies perturb the horizontal flow, leading to regions where u varies by 10 m s^{-1} over a distance of only 7 km.

The variations in vertical velocity (Fig. 10) show that the Type 2 rotor is more hazardous for aviation. At a height of 7 km, an aircraft transitioning the Type 2 rotor would encounter horizontal shear in vertical velocity at least four times greater than at the same height in the Type 1 system. In the Type 1 system, an aircraft at 7 km would also be above rotor turbulence. Vertical motions in the Type 2 rotor, some exceeding 10 m s^{-1}, continue downstream of the mountain crest for at least 50 km. Particularly, strong horizontal shear of the vertical velocity occurs at the leading edge of the Type 2 rotor at heights between 5 and 6 km. Other Type 2 simulations provide short-lived vertical velocities exceeding 20 m s^{-1}.

Horizontal vorticity, $\eta = (\partial u/\partial z) - (\partial w/\partial x)$, bulk Richardson number (Ri), and subgrid-scale turbulent kinetic energy (TKE) further illustrate differences between S1 and S2 rotors. The mountain in our simulations is assumed to be aligned north–south. Thus, positive horizontal vorticity (η_+) is associated with clockwise circulation, and negative horizontal vorticity (η_-) with counterclockwise circulation (Fig. 11). The S1 rotor consists mostly of η_+, which is lifted at a boundary layer separation point and becomes partially entrained in the primary rotor (Fig. 11a), while η_- is confined to wave troughs and small areas within the rotor itself. By contrast, η_- is far more widespread within the S2 rotor (Fig. 11b). Maximum η_+ in S2 occurs along the rotor leading edge. The downstream propagating eddies near the S2 rotor top are also obvious as three distinct areas of η_+.

Differences in the spatial extent of turbulence between the two rotor types are illustrated by inspection of regions with Ri < 0.25, a commonly used threshold for turbulent flows. The more confined areas of turbulence in S1 are readily seen in Fig. 12; very little turbulent flow is evident in S1 above 4 km. By contrast, turbulent flow in S2 extends to 7.5 km, and is spatially more variable, again emphasizing the aviation hazard of the Type 2 rotor.

Turbulence is far more intense and temporally variable in the S2 rotor compared to S1. Figure 13 shows maximum TKE for each simulation calculated between $x = 20$ and 40 km, and up to $z = 8$ km (see, for example, Fig. 12) at 1-min intervals. Maximum TKE in S1 changes little from 10 m^2 s^{-2}, while in S2 maximum TKE is generally stronger and fluctuates between about 10 and 48 m^2 s^{-2}.

In summary, the simulated Type 2 rotor occurs in conjunction with a mountain-wave system resembling a hydraulic jump, and has a fundamentally different structure than the Type 1 rotor, which occurs in association with resonant waves. The Type 2 rotor exhibits a steeper leading edge, and an inversion that splits at the jump. In agreement with observations (e.g. Kuettner, 1959; Lester and Fingerhut, 1974) the S2 simulation produces a type of rotor that is vertically more extensive, with stronger turbulence than found in Type 1 rotors. Based on the experience of SWP and JSP pilots, it is possible that the rotor in Fig. 5 is Type 2. The rotor in S2 has an extensive area of negative horizontal vorticity, as well as elevated propagating eddies with positive vorticity, although these characteristics have yet to be verified from observations.

4. Horizontal vorticity evolution and rotor formation

In this section, we explore the mechanisms leading to the formation of the Type 1 and Type 2 rotors. The rotor formation can be understood from the evolving horizontal vorticity which was calculated from model output at 30-s intervals. As a note, sensitivity studies were run with wind spin-up times varying from 5 to 30 min. A similar evolution and the same final solution (i.e. a Type 1 versus Type 2 rotor) occurred in each case regardless of wind spin-up time used.

During the first several minutes of each simulation, the flow begins a cascade down the lee slope, and isentropes in the near-mountain-top inversion are deflected sharply downwards. Differences in the initial shear through the inversion lead to important differences in the two simulations. The total tendency of η for a two-dimensional, Boussinesq system (with $f = 0$, and compressibility neglected) is given by

$$\frac{d\eta}{dt} = B_x + D$$

where $B_x = -g(\partial/\partial x)(\theta'/\bar{\theta})$, $\theta = \bar{\theta}(z) + \theta'$, and D represents subgrid-scale turbulent stresses. The first term on the right-hand side represents baroclinic generation through horizontal buoyancy gradients. In the first several minutes of the simulation, B_x develops quickly within the inversion and becomes anchored along the lee slope, leading to production of negative horizontal

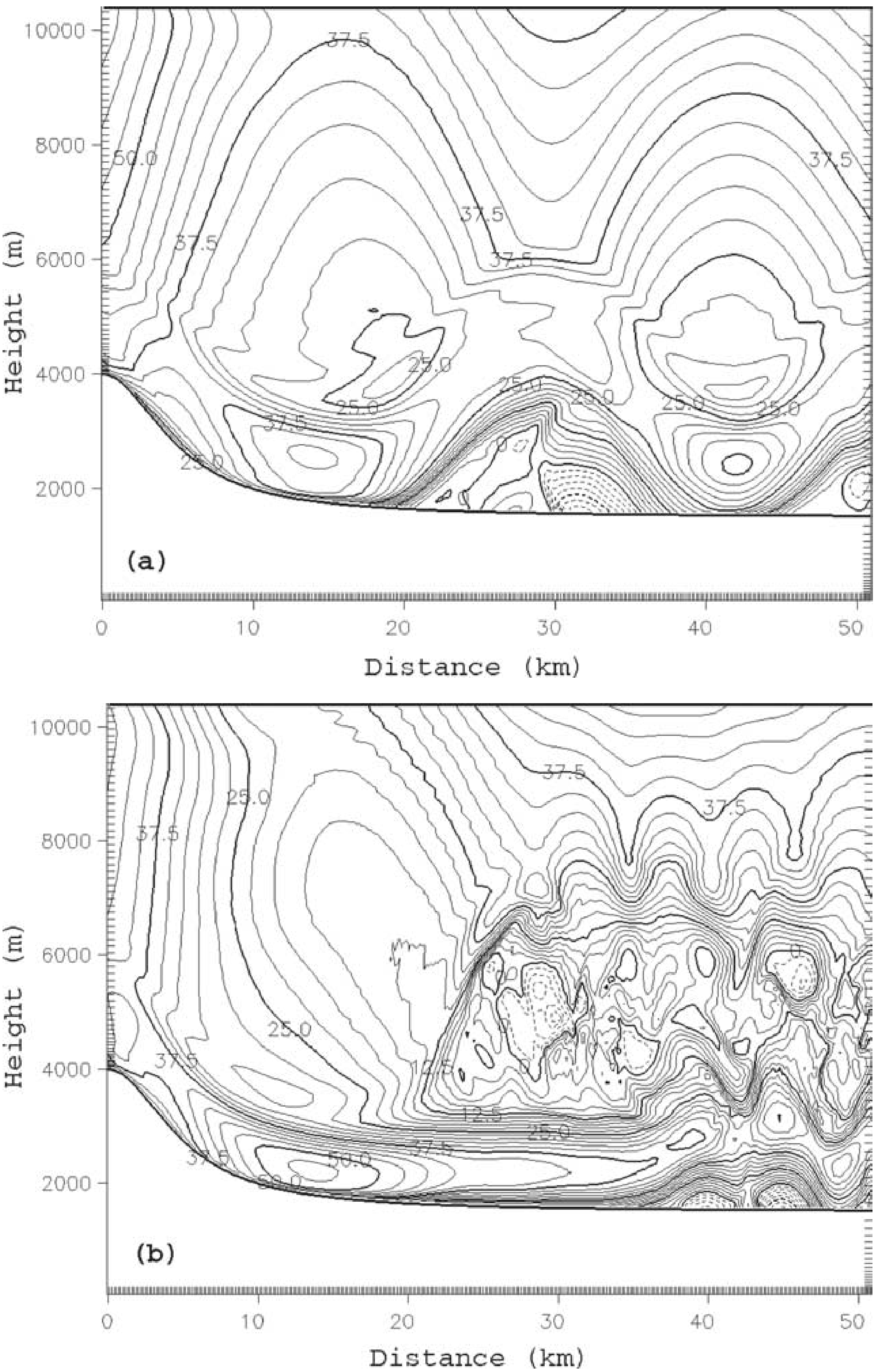

Fig 9. As Fig. 7, except for horizontal velocity, *u* (contour interval 2.5 m s^{-1}). Negative *u* is dashed. Note near-surface reversed flow in S1. Extended near-surface jet occurs in S2, along with elevated regions of reversed flow.

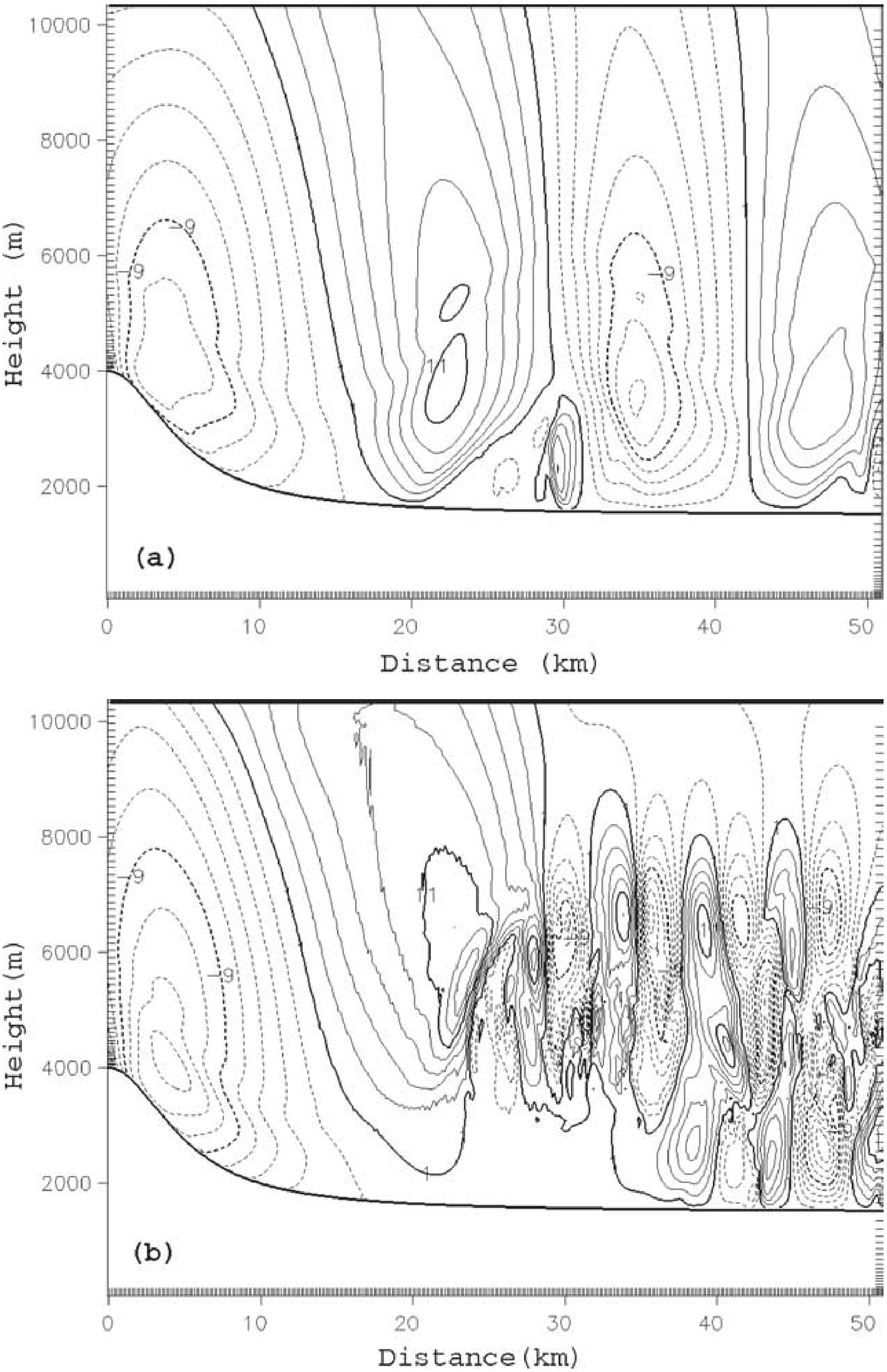

Fig 10. As in Fig. 7, except for vertical velocity, w (contour interval 2 m s^{-1}). Negative w is dashed and the zero contour line has been deleted. Vertical velocities exceed ±11 m s^{-1} at a height near 7 km in S2.

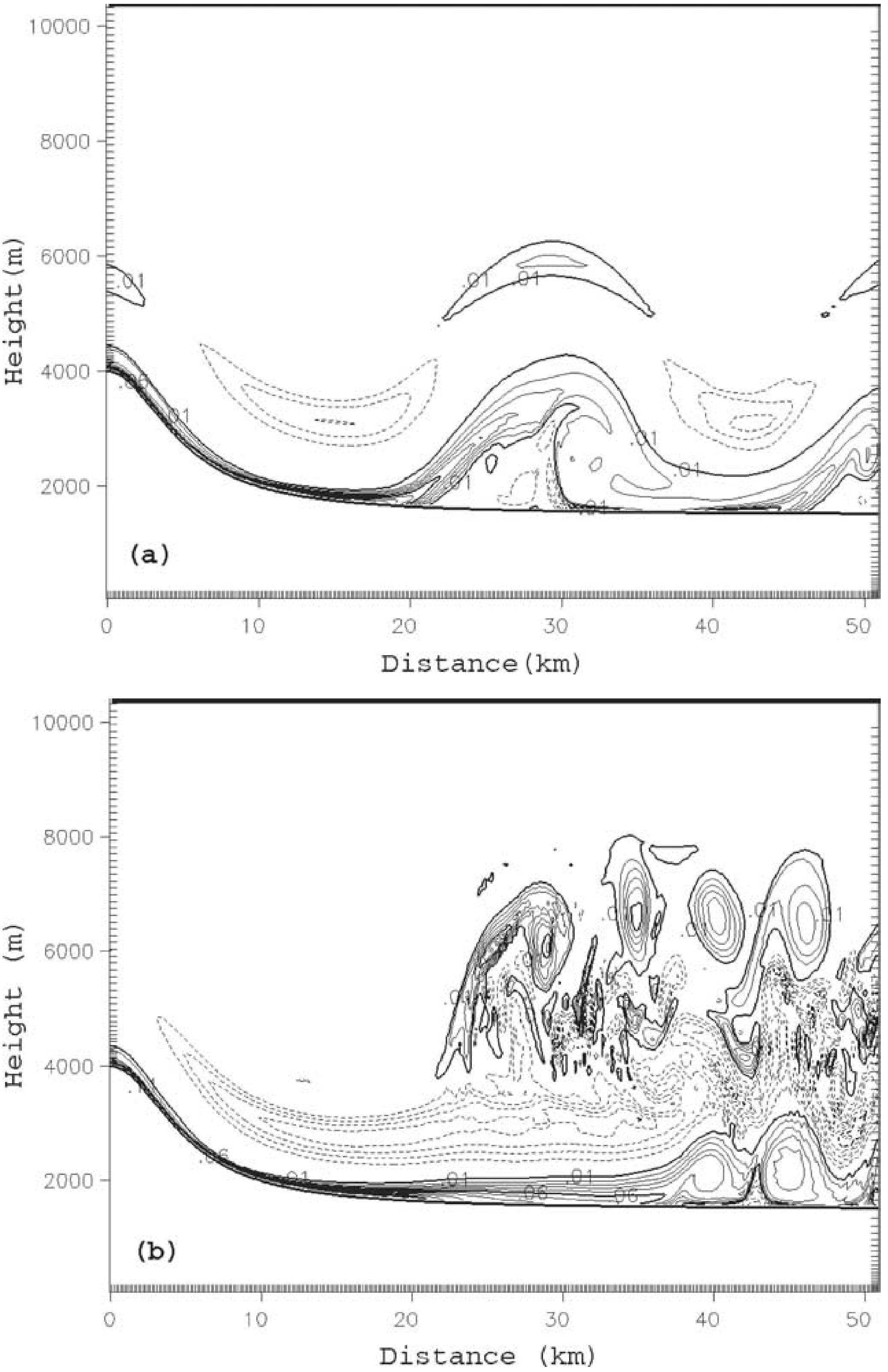

Fig 11. As Fig. 7, except for horizontal vorticity, η (contour interval 0.01 s^{-1}). Negative η is dashed and the zero contour line has been deleted for clarity. Negative vorticity is far more extensive in S2. Maximum positive vorticity along the Type 2 rotor leading edge is 0.07 s^{-1}.

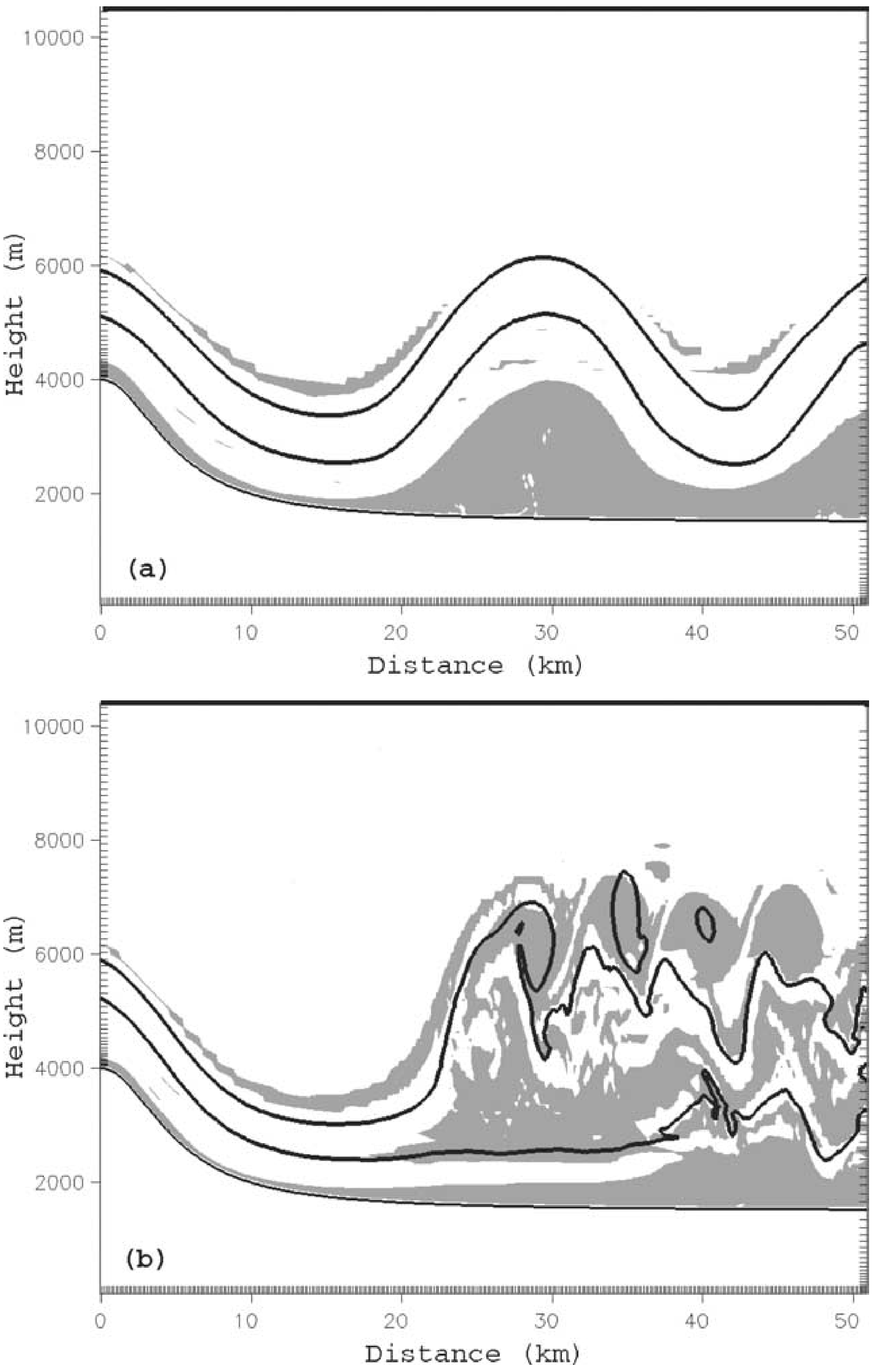

Fig 12. Richardson number (Ri < 0.25 shaded) and the 301 K (lower) and 312 K (upper) isentrope (solid lines) which bound the upstream inversion: (a) Type 1 rotor; (b) Type 2 rotor. Model time is 3 h as in previous figures.

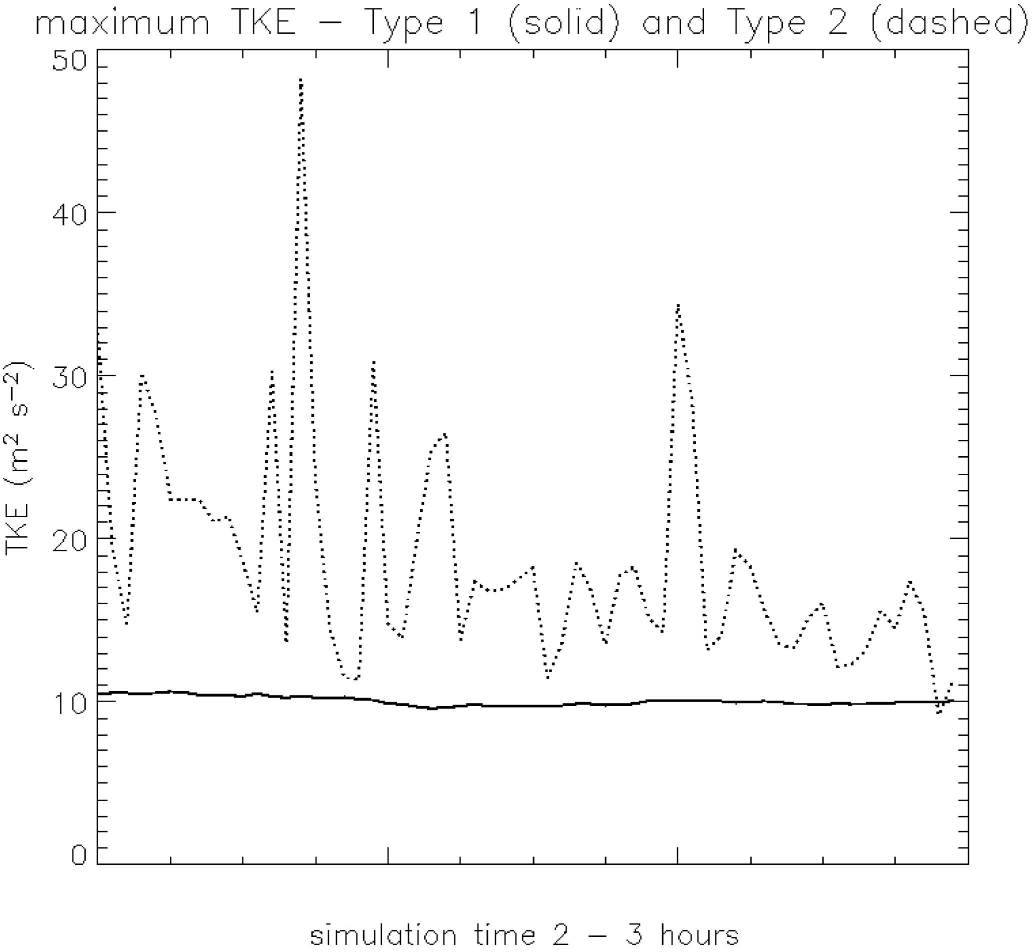

Fig 13. Time series (between two and three hours) of maximum subgrid-scale TKE within each rotor. Maximum is calculated from model output at 1-min intervals. Little variation is seen for the Type 1 rotor (solid line) while more intense and volatile maximum TKE occurs in the Type 2 rotor (dashed line).

vorticity. At the same time, in the lowest model levels, positive horizontal vorticity is produced in the shallow surface layer along the lee slope.

After 12-min model integration, baroclinic generation is only 10% stronger for Type 2 than Type 1, but η_- is much stronger (Fig. 14). This is not surprising because B_x occurs almost entirely within the inversion. In the Type 1 simulation, B_x modifies an initial positive horizontal vorticity of 13.3×10^{-3} s^{-1} while in the Type 2 simulation, B_x modifies initially zero horizontal vorticity. Other smaller and transient areas of B_x occur near 4.5 km due to the developing mountain wave. At this time, boundary layer separation has begun (at approximately $x = 11$ km in Fig. 14), resulting in horizontal vorticity of both signs being lifted. In both simulations, positive horizontal vorticity between 4 and 5 km is associated with the deformed inversion due to the developing mountain wave and is not connected to the surface layer. For Type 2, a counterclockwise rotor circulation forms in association with the dominant negative horizontal vorticity. Indeed, at this time a small but growing area of negative u has already formed at $x = 11$ km, and $z = 4.2$ km (not shown).

Figure 15 shows the model integration at 22 min. For Type 1, the dominant positive horizontal vorticity has caused the flow to curl downstream, carrying with it horizontal vorticity of both signs. By contrast, for Type 2, a portion of the flow has curled upstream to create an eddy with negative horizontal vorticity. Up to this time, the S2 evolution has resembled that simulated by Rotunno and Smolarkiewicz (1995).

The two types of rotor have already become established at this relatively early simulation time. At subsequent times, the Type 1 rotor maintains steadily turbulent, (e.g. Fig. 13) nearly neutrally stable air below each wave crest. The flow within the Type 2 rotor is much less steady, leading to fluctuating turbulence intensities, and sharp gradients in vertical and horizontal winds. Type 1 rotors occur when the magnitude of surface-layer positive horizontal vorticity lifted during flow separation exceeds the magnitude of negative horizontal vorticity that is baroclinically

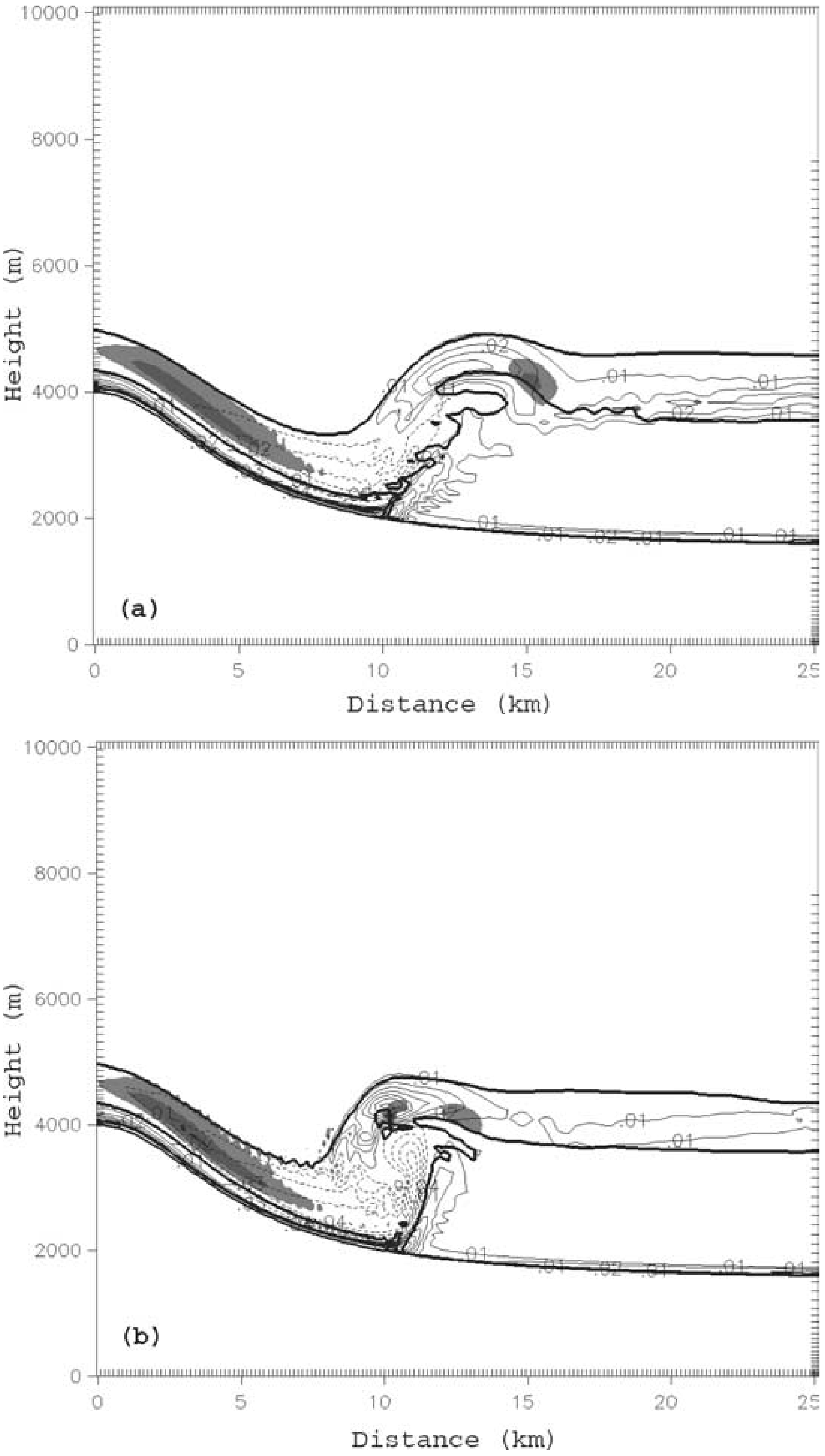

Fig 14. Horizontal vorticity (thin contours, interval 10^{-2} s^{-1}, negative values dashed) at 12 min for (a) Type 1 rotor and (b) Type 2 rotor. Zero contour not shown for clarity. Horizontal vorticity generation (B_x) less than -1.0×10^{-4} s^{-2} shaded, with minimum B_x of -2.7×10^{-4} s^{-2} for Type 1 and -3.0×10^{-4} s^{-2} for Type 2. Thick contours indicate the top (312 K) and bottom (301 K) isentropes bounding the upstream inversion. Negative horizontal vorticity is twice as strong for Type 2.

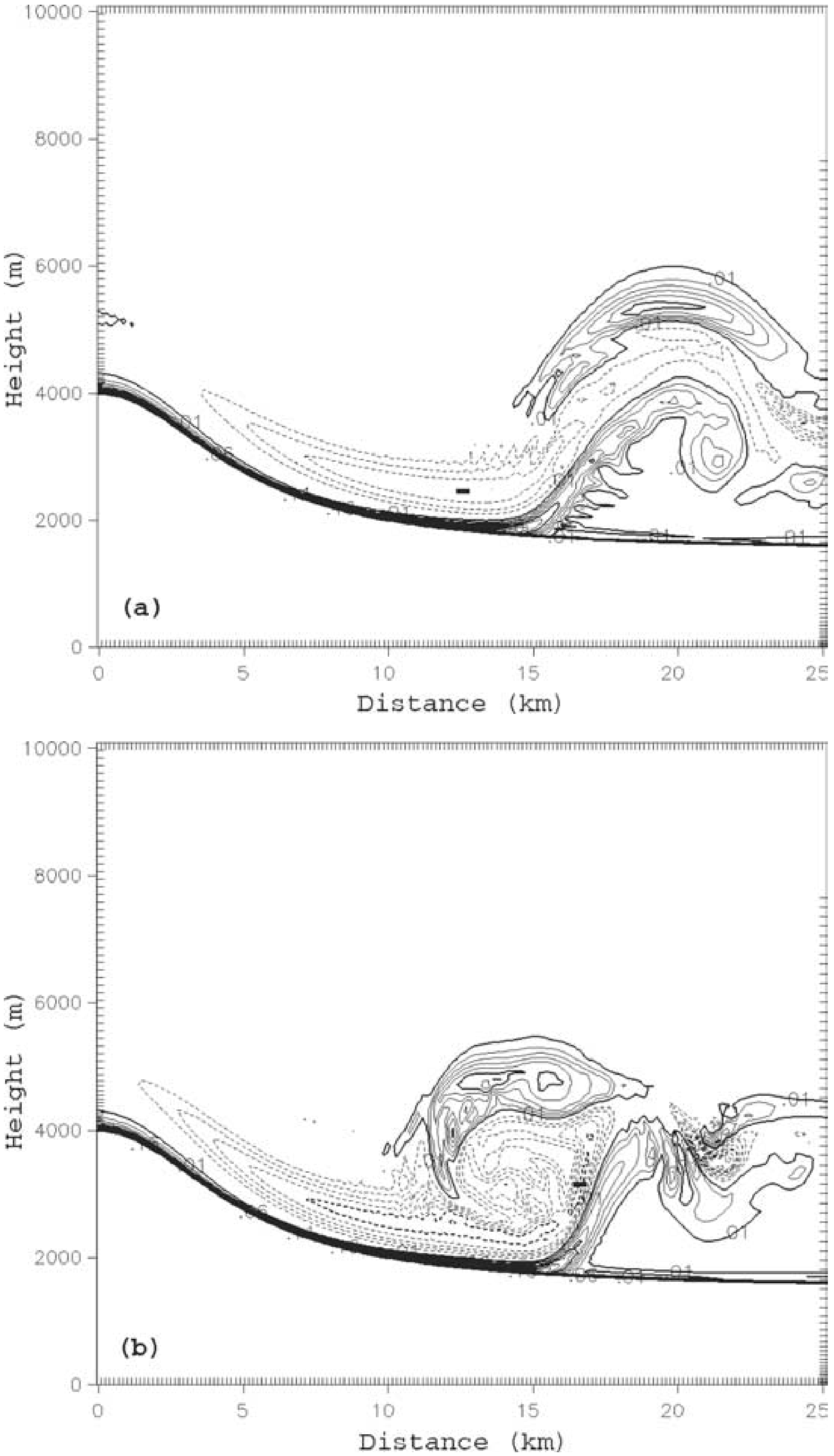

Fig 15. Horizontal vorticity at 22 min (contour interval 0.01 s^{-1} and negative values dashed). (a) Both positive and negative horizontal vorticity continue to curl downstream with the flow. The '−' indicates minimum horizontal vorticity of -3.6×10^{-2} s^{-1}. (b) Flow has curled upstream and now forms an eddy with negative horizontal vorticity which causes leading-edge positive vorticity to steepen. The '−' indicates minimum horizontal vorticity of -5.5×10^{-2} s^{-1}.

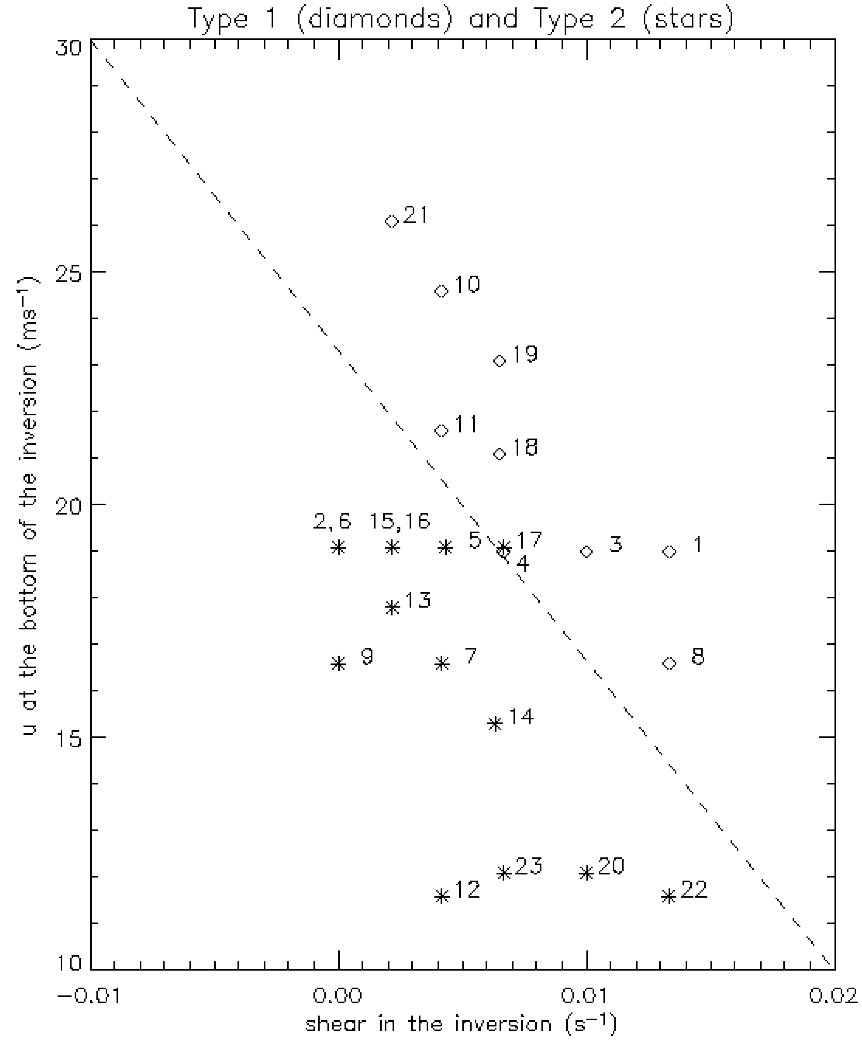

Fig 16. Scatter plot showing initial flow at bottom of the inversion versus initial shear through the inversion. Simulation number indicated next to symbol. Simulations 1 and 2 are, respectively, S1 and S2 shown in Fig. 7. Note that simulated Type 1 rotors (diamonds) occur with stronger initial shear and flow (above the dotted diagonal), while simulated Type 2 rotors (stars) occur with weaker initial shear and flow (below the diagonal).

generated along the lee slope. By contrast, Type 2 rotors occur when the magnitude of negative horizontal vorticity exceeds the magnitude of positive horizontal vorticity.

5. Discussion

In this section, we present results from a series of simulations designed to further explore the sensitivity to the magnitude of the shear through the inversion and speed of the near-mountain-top flow.

5.1. *Role of the wind profile*

Twenty-one additional simulations were completed, all of which used the same topography and potential temperature profile as S1 and S2, but with modifications to the wind profile. A scatter plot of initial flow at the bottom of the inversion versus the shear through the inversion reveals a clear division between conditions leading to Type 1 and Type 2 rotors (Fig. 16). Simulations 1 and 2 are, respectively, S1 and S2 discussed earlier (see, for example, Fig. 7). Type 1 rotors occur with stronger shear through the inversion along with stronger near-mountain-top initial flow (i.e. above the diagonal) while Type 2 rotors occur in weaker shear along with weaker near-mountain-top flow (i.e. below the diagonal).

Simulations 4 and 17 are collocated, indicating that in this parameter space they represent a transition zone between Type 1 and Type 2 rotors. The two simulations differ in the wind profile above the inversion. Stronger vertical shear above the inversion in simulation 4 leads to maximum flow of 51 m s^{-1} at the tropopause, while weaker vertical shear above the inversion in simulation 17 leads to maximum flow of 34 m s^{-1} at the tropopause. Conditions are thus more favorable for trapped waves in simulation 4. These two simulations imply that characteristics of the flow above the inversion (e.g. magnitude of the vertical shear) have an influence on the rotor type. However, we were not able to find a consistent correlation between flow characteristics above and below the inversion.

An inverse relationship was found between the average initial flow in the near-mountain-top inversion and the resulting baroclinic generation of horizontal vorticity. As the flow near the mountain top increases, the magnitude of B_x decreases. Thus, somewhat to our surprise, Type 1 rotors generally formed in stronger near-mountain-top flow while Type 2 rotors formed in weaker flow. In the simulations, B_x with magnitude greater than 3.0×10^{-4} s^{-2} generally led to the formation of Type 2 rotors.

The results of the sensitivity experiments are consistent with the findings of Section 4. It must be stressed again that these results apply only to the topography and strong inversion used in our simulations. Work is underway to explore the role of the inversion strength, depth, and height, as well as different topography profiles, including the effect of mountains further downstream. Our results suggest that knowledge of the near-mountain-top flow and shear through the inversion may provide a useful forecast tool.

5.2. *Sensitivity to the turbulence parametrization*

As described in Section 2, turbulence was parametrized using the Deardorff (1980) scheme. In order to eliminate the possibility that the results were fundamentally dependent on the turbulence scheme, we also performed simulations using the S1 and S2 wind and stability profiles, but with three alternative turbulence schemes available in RAMS. The first alternative scheme uses the Mellor and Yamada (1974) scheme for vertical mixing. Numeric stability is achieved following Smagorinsky (1963); horizontal diffusion coefficients are calculated from the horizontal deformation rate multiplied by a length-scale, which is a function of the horizontal grid spacing. The second alternative scheme also follows Smagorinsky (1963) to treat horizontal diffusion. Vertical diffusion is calculated in an analogous way using the product of vertical deformation and a vertical length-scale, which is a function of the vertical grid spacing. Modifications to this scheme in the vertical are based on the formulations of Hill (1974) and Lilly (1962). The third alternative scheme computes horizontal and vertical diffusion coefficients from the product of a three-dimensional rate-of-strain tensor and a length-scale (which is a function of the vertical grid spacing) squared. The Hill (1974) and Lilly (1962) modifications are applied to this alternative scheme as well.

Regardless of the turbulence parametrization used, the S1 sounding always produced a Type 1 rotor, while the S2 sounding always produced the Type 2 rotor.

6. Conclusions

We have simulated two types of rotors by systematically varying the shear in the upstream inversion. The two rotor types form distinctly different flow and turbulence characteristics. Simulated Type 1 rotors are the more-familiar type that form under resonant mountain-wave crests with an upstream near-mountain-top inversion that undulates, but remains intact downstream of the mountain (Fig. 7a). By contrast, simulated Type 2 rotors form in association with mountain waves that resemble a hydraulic jump and are characterized by turbulent flow extending 3.5 km above the mountain top and for more than 50 km downstream (Fig. 7b). The initial upstream inversion splits at the downstream jump, which may explain the greater height achieved by Type 2 rotors and also illuminates a possible flow regime within high-reaching and extremely turbulent rotors, as shown in Fig. 5. It is hoped that observations taken during the up-coming T-REX (Grubišić and Kuettner, 2003) will reveal details of the internal structure of rotors.

Simulated Type 1 rotors display a rather consistent maximum TKE of the order of 10 m^2 s^{-2}. On the other hand, within simulated Type 2 rotors, TKE varies between 10 and 48 m^2 s^{-2} as individual eddies form and propagate downstream through the rotor (Fig. 13). Plots of the Richardson number (Fig. 12) reveal a rather uniformly turbulent region primarily below wave crests of simulated Type 1 rotors, while turbulence reaches greater heights and varies more in space and time in simulated Type 2 rotors.

The simulations attest to the vital role of an upstream near-mountain-top inversion, its deformation in the lee of the mountain, and the initial vertical shear within the inversion. The simulated rotor type depends on the sign of the dominant horizontal vorticity as boundary-layer flow separation occurs along the lee slope. Negative horizontal vorticity is produced along the lee slope by baroclinic generation as the upstream inversion becomes deformed in the lee of the mountain. At the same time, positive horizontal vorticity forms in the surface layer along the lee slope. As boundary layer separation occurs, horizontal vorticity of both signs is lifted. Positive vorticity dominates the evolving Type 1 rotor while negative vorticity dominates the evolving Type 2 rotor.

A series of sensitivity runs underscores the consistency of our results (Fig. 16). Stronger shear through the inversion along with stronger near-mountain-top flow leads to simulated Type 1 rotors. Conversely, weaker shear through the inversion along with weaker near-mountain-top flow leads to simulated Type 2 rotors. Increased baroclinic generation also occurs with weaker near-mountain-top flow, leading to greater negative horizontal vorticity associated with simulated Type 2 rotors.

Flow regimes likely exist in nature that are different from either the Type 1 and Type 2 rotors simulated here, especially if considering more complex, three-dimensional mountain ranges. The flow structure within the Type 2 rotor has not been shown by observations. This is due to the fact that, with the exception of numerous anecdotal accounts by pilots, few quantitative observations exist. However, some of the simulated Type 2 characteristics, namely their greater height and turbulent intensity, have been observed (Kuettner, 1959; Lester and Fingerhut, 1974) in both the Sierra Nevada and Rocky Mountains.

Results reported herein were obtained by varying only the initial wind profile; stability profiles and topography were not modified. Work is currently underway to investigate modifications to the rotor due to changes in the near-mountain-top inversion (e.g. inversion depth, strength, and height in relation to the mountain top). Further simulations are also underway to investigate and quantify the role of the lee slope shape and height, as well as the influence of downstream topography, in rotor formation.

Two-dimensional simulations cannot completely treat what in nature is a fully three-dimensional phenomenon. For instance, vorticity tilting and stretching mechanisms are not possible in two dimensions. Further structure, such as small-scale subrotors, would probably be simulated with finer grid spacing. Thus, the simulations presented here likely do not capture the full intensity of rotors occurring in nature. Nonetheless, these two-dimensional simulations lay the foundation for future three-dimensional modeling and observational studies. In addition, the results may provide useful guidance for forecasting rotor intensity based on inversion strength and shear through the inversion based on inspection of a sounding taken upstream of the mountains.

7. Acknowledgments

Ms Becky Meitin is thanked for her assistance with editing the final manuscript and Mr Brian Laughman for his help with preparation of the figures. Two anonymous reviewers provided insightful comments which improved the manuscript. This research was supported by the National Science Foundation under grant ATM-0233165.

References

Clark, T. L., Hall, W. D., Kerr, R. M., Middleton, D., Radke, L. et al. 2000. Origins of aircraft-damaging clear-air turbulence during the 9 December 1992 Colorado downslope windstorm: numerical simulations and comparison with observations. *J. Atmos. Sci.* **57**, 1105–1131.

Deardorff, J. W. 1980. Stratocumulus-capped mixed layers derived from a three-dimensional model. *Bound.-Layer Meteorol.* **18**, 495–527.

Doyle, J. D. and Durran, D. R. 2002. The dynamics of mountain-wave-induced rotors. *J. Atmos. Sci.* **59**, 186–201 (DD).

Doyle, J. D. and Durran, D. R. 2003. Rotor dynamics in the lee of three-dimensional ridges. Paper 11.4, *Tenth AMS Conference on Mesoscale Meteorology*, American Meteorological Society, Portland OR, USA. Available online from the American Meteorological Society at http://ams.confex.com/ams/htsearch.cgi.

Durran, D. R. and Klemp, J. B. 1982. The effects of moisture on trapped mountain waves. *J. Atmos. Sci.* **39**, 2490–2506.

Foerchtgott, J. 1949. Rotor streaming in the lee of mountain ridges. *Bull. Met. Czech. Prague* **4**, 14–16.

Foerchtgott, J. 1969. Evidence for mountain-sized lee eddies. *Weather* **24**, 255–260.

Grubišić, V. and Kuettner, J. P. 2003. Terrain-Induced Rotor Experiment (T-REX). Paper 11.3, *Tenth AMS Conference on Mesoscale Meteorology,* American Meteorological Society, Portland, OR, USA. Available online from the American Meteorological Society at http://ams.confex.com/ams/htsearch.cgi.

Grubišić, V. and Lewis, J. M. 2004. Sierra Wave Project revisited: 50 years later. *Bull. Am. Meteorol. Soc.* **85**, 1127–1142.

Hill, G. E. 1974. Factors controlling the size and spacing of cumulus clouds as revealed by numerical experiments. *J. Atmos. Sci.* **31**, 646–673.

Holmboe, J. and Klieforth, H. 1957. Investigation of mountain lee waves and the air flow over the Sierra Nevada, Contract No. AF19(604)-728, Department of Meteorology, UCLA, USA, 290 pp.

Kahn, B. H., Chan, W. and Lester, P. F. 1997. An investigation of rotor flow using DFDR data. In: *Proceedings of the 7th Conference on Aviation, Range, and Aerospace Meteorology,* American Meteorological Society, Long Beach, CA, USA, 206–210.

Klemp, J. B. and Lilly, D. K. 1978. Numerical simulations of hydrostatic mountain waves. *J. Atmos. Sci.* **35**, 78–106.

Koschmieder, H. 1920. Zwei bemerkenswerte Beispiele horizontaler Wolkenschlaeuche. *Beitr. Phys. fr. Atm.* **9**, 176–180.

Kuettner, J. 1959. The rotor flow in the lee of mountains. Geophysics Research Directorate (GRD) Research Notes 6, AFCRC-TN-58-626, Air Force Cambridge Research Center, USA, 20 pp.

Kuettner, J. and Hertenstein, R. F. 2002. Observations of mountain-induced rotors and related hypotheses: a review. In: *Proceedings of the 10th AMS Conference on Mountain Meteorology,* American Meteorological Society, Park City, UT, USA, 326–329.

Lester, P. F. 1994. *Turbulence: A New Perspective for Pilots*. Jeppensen Sanderson Training Products, Englewood, Colorado, USA, 212 pp.

Lester, P. F. and Fingerhut, W. A. 1974. Lower turbulent zones associated with lee waves. *J. Appl. Meteorol.* **13**, 54–61.

Lilly, D. K. 1962. On the numerical simulation of buoyant convection. *Tellus* **14**, 148–172.

Lilly, D. K. and Toutenhoofd, W. 1969. The Colorado Lee Wave Program. In: *Clear Air Turbulence and Its Detection* (eds Y. Pao and A. Goldburg). Plenum Press, New York, 232–245.

Louis, J. F. 1979. A parametric model of vertical eddy fluxes in the atmosphere. *Bound.-Layer Meteor.* **17**, 187–202.

Mellor, G. L. and Yamada, T. 1974. A hierarchy of turbulence closure models for planetary boundary layers. *J. Atmos. Sci.* **31**, 1791–1806.

National Transportation Safety Board (NTSB), 1992. Report Number DEN93FA017, http://nasdac.faa.gov/asp/fw_ntsb.asp

Pielke, R. A., Cotton, W. R., Walko, R. L., Tremback, C. J., Lyons, W. A. et al. 1992. A comprehensive meteorological modeling system – RAMS. *Meteorol. Atmos. Phys.* **49**, 69–91.

Poulos, G. S., Bossert, J. E., Pielke, R. A. and McKee, T. B. 2000. The interaction of katabatic flow and mountain waves I: observations and idealized simulations. *J. Atmos. Sci.* **57**, 1919–1936.

Ralph, F. M., Neiman, J., Kellor, T. L., Levinson, D. and Fedor, L. 1997. Observations, simulations and analysis of non-stationary trapped lee waves. *J. Atmos. Sci.* **54**, 1308–1333.

Rotunno, R. and Smolarkiewicz, P. 1995. Vorticity generation in the shallow-water equations as applied to hydraulic jumps. *J. Atmos. Sci.* **52**, 320–330.

Smith, R. B. 1987. Aerial observations of the Yugoslavian bora. *J. Atmos. Sci.* **44**, 269–297.

Smagorinsky, J. 1963. General circulation experiments with the primitive equations. Part I: the basic experiment, *Mon. Wea. Rev.* **91**, 99–164.

Worthington, R. M. 2002. Mountain waves launched by convective activity within the boundary layer above mountains. *Bound.-Layer Meteorol.* **103**, 469–491.